2 Instrumentation and data analysis

2.1 The Solar and Heliospheric Observatory

The Solar and Heliospheric Observatory (SOHO) was launched on December 2nd, 1995. It is a collaborative effort between the European Space Agency (ESA) and the National Aeronautics and Space Administration (NASA) to study the Sun, from its deep core to the outer corona, and the solar wind. The principal scientific objectives of the SOHO mission can be summarized:

- Study of the structure and dynamics of the solar interior, using the techniques of helioseismology
- Study of the heating mechanisms of the solar corona
- Investigation of the solar wind and its acceleration processes.

Proposed in November 1982, SOHO inherits the scientific objectives of earlier studies which had to be abandoned, namely GRIST (Grazing Incidence Solar Telescope) and DISCO (Dual Spectral Irradiance and Solar Constant Orbiter). On February 1986, SOHO was approved as the first mission of the first cornerstone of ESA's long-term programme "Space Science Horizon 2000", fully devoted to studying the Sun. Thirteen years after its proposal, the SOHO spacecraft was shipped from Toulouse to Kennedy Space Center at Cape Canaveral. It was finally launched on an ATLAS II-AS rocket in December 1995, reaching its final location on 14 February 1996. Figure 2.1 provides a schematic view of the SOHO spacecraft, and its main characteristics are summarized in table 2.1.

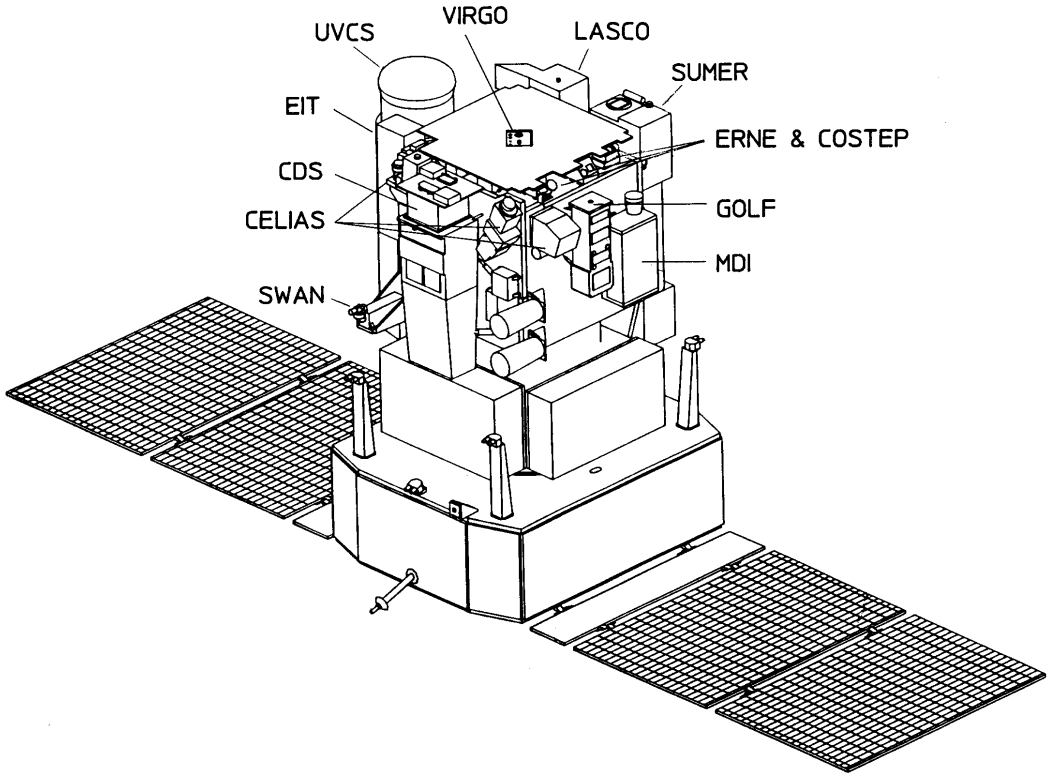

Figure 2.1: SOHO spacecraft schematic view

SOHO was injected into a transfer orbit to the Sun-Earth L1 Lagrangian point, about 1.5 10^6 km (1% AU) sunward from the Earth. After a transfer phase of approximately 4 months, the spacecraft was injected into a halo orbit around L1, where it continuously points to Sun center with an accuracy of 10″. Pointing stability is better than 1″ over 15 min intervals. Its orbit can be seen in figure 2.2. Table 2.1 shows the parameters of this halo orbit. The L1 halo orbit has several particular advantages as compared to low Earth orbits: a) it provides a smooth Sun-spacecraft velocity change throughout the orbit, required to obtain accurate helioseismology measurements, b) it is permanently outside the magnetosphere, appropriate for the *in situ* sampling of the solar wind and particles, and c) it allows uninterrupted observation of the Sun, appropriate for all the investigations.

The scientific payload of SOHO comprises twelve state-of-the-art instruments developed by twelve international consortia involving 39 institutes from 15 countries. The experiments on board SOHO can be divided into three main groups, according to their area of research: helioseismology instruments, solar corona instruments and

Table 2.1: The SOHO Mission

Mission objectives	Investigations of the Sun, from its interior to, and including, the solar wind
Mission shares	ESA: spacecraft plus 9 experiments by member states NASA: launcher, ground segment plus 3 experiments
Launch	2 December 1995
Mission lifetime	$\geq$ 2 years (on-board consumables for up to 6 years)
Size	$4.3 \times 2.7 \times 3.7\,\mathrm{m}^3$
Mass	total: 1861 kg (payload: 655 kg; propellants: 250 kg)
Power	1400 W (maximum supply from solar cells) payload (mean/max): 440/625 W
Data rate	scientific (continuous): 40 kbits/s MDI high rate (part time): 160 kbits/s housekeeping: 1.3 kbits/s
Data storage	2 Gbits (Solid State Memory) + 1 Gbit (Tape Recorder)
Telemetry rate	245.8, 54.6 and 1.4 kbits/s (high/medium/low rate)
Orbit	halo orbit around L1
semi diameters	(x) (within ecliptic, earth-Sun) $\approx$ 200.000 km (y) (within ecliptic) $\approx$ 650.000 km (z) (out of ecliptic) $\approx$ 200.000 km
period	6 months
Attitude control	3-axis stabilization
Telemetry and tracking	26 m (primary) and 34 m DSN stations in Canberra, Madrid and Goldstone

solar wind instruments. Helioseismology experiments aim to obtain high sensitivity observations of low order solar p (pressure) and $-$ if detectable $-$ g (gravity) mode oscillations, as well as intermediate to very high degree $p-$modes, in order to deduce the solar structure from the surface through the deep core. Coronal instruments study the physical properties of the solar corona by measuring the temperature, density, velocity and turbulence of the inner and outer corona. Finally, the last group of experiments measure the composition of the solar wind and energetic particles, determining the elemental and isotopic abundances, the ionic charge states and velocity distributions of ions originating in the solar atmosphere. A brief summary of the scientific payload is given in table 2.2. More details about the SOHO mission can be found in Domingo et al. (1995).

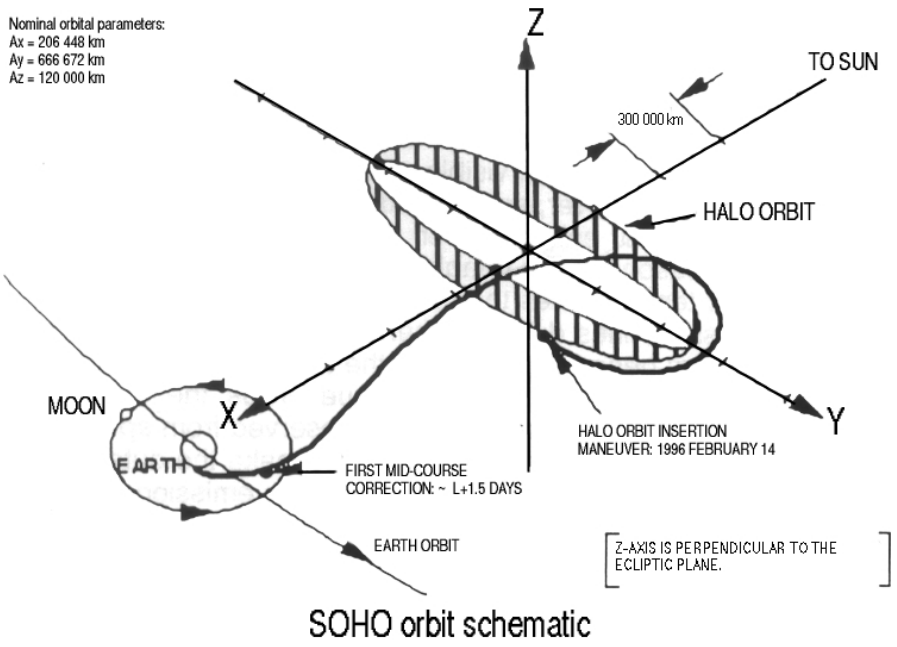

Figure 2.2: SOHO orbit

Since April 1998 SOHO observations have been complemented by those of TRACE (Transition Region And Coronal Explorer), a NASA ultraviolet telescope designed to explore the connections between fine-scale magnetic fields at the solar surface and the associated plasma structures in the solar outer atmosphere with 1″ resolution. The TRACE mission and its objectives are described in detail in Handy et al. (1999). Planning of the daily TRACE observations is coordinated with those of SOHO.

The telemetry of the satellite was lost on 25 June 1998 and no communication was possible between ground controllers and the spacecraft. An ESA/NASA investigative board identified three separate causes for the accident (see Appendix A), which apparently sent the spacecraft into a spin that misaligned its communications antenna and turned its solar panels away from the Sun. After three months of hard work by the recovery team, the spacecraft could finally be located using the Deep Space Network Arecibo antenna. Operations to recover the telemetry and check the general status of the spacecraft started. SOHO was back in normal mode again on 25 September 1998. All instruments were successfully recovered without damage, despite the enormous gradient of temperatures between the sunny and the dark sides of the satellite. Only two of the three gyroscopes were lost during these operations;

Table 2.2: SOHO Scientific Instruments

(The highlighted instruments will be described in more detail in the next sections)

Investigation	Measurements	Principal Investigators
HELIOSEISMOLOGY		
GOLF	Global Sun velocity oscillations (l=0-3)	A. Gabriel (IAS, France)
VIRGO	**Low degree (l=0-7) irradiance oscillations and solar constant**	**C. Fröhlich (PMOD, Switzerland)**
MDI/SOI	**Velocity oscillations, harmonic degree up to 4500**	**P. Scherrer (Stanford Univ., USA)**
SOLAR ATMOSPHERE REMOTE SENSING		
SUMER	Plasma flow characteristics (T, density, velocity) chromosphere through corona	K. Wilhelm (MPAe, Germany)
CDS	Temperature and density: transition region and corona	R. Harrison (RAL, UK)
EIT	Evolution of chromospheric and coronal structures	J.-P. Delaboudinière (IAS, France)
UVCS	Electron and ion temperature, densities, velocities in corona (1.3-10 $R_\odot$)	J. Kohl (SAO, USA)
LASCO	Evolution, mass, momentum and energy transport in corona (1.1-30 $R_\odot$)	G. Brueckner (NRL, USA)
SWAN	Solar wind mass flux anisotropies and its temporal variations	J.-L. Bertaux (SA, France)
SOLAR WIND		
CELIAS	Energy distribution and composition (mass, charge, chargestate)(0.1-1000 keV/e)	Hardware phase: D. Hovestadt (MPE, Germany) Data phase: P. Bochsler (University of Bern, Switzerland)
COSTEP	Energy distribution of ions (p, He) 0.04-53 MeV/n and electrons 0.04-5 MeV	H. Kunow (University of Kiel, Germany)
ERNE	Energy distribution and isotopic composition of ions (p-Ni) 1.4-540 MeV/n and electrons 5-60 MeV	J. Torsti (University of Turku, Finland)

the third failed over in December 1998. It was then necessary to upload gyroless software that uses reaction wheels to measure the spacecraft roll. SOHO has become the first 3-axis stabilized spacecraft to be operated without a gyroscope.

2.1.1 The VIRGO experiment

VIRGO (Variability of solar IRradiance and Gravity Oscilations) provides continuous high-precision and high-stability measurements of the solar total and spectral irradiance and spectral radiance variations, continuous measurements of the solar polar and equatorial diameter, and frequencies, amplitudes and phases of oscillation modes in the frequency range of 1 μHz to 8 mHz. More details about the VIRGO experiment and its sensors can be found in Fröhlich et al. (1995).

Among the main scientific objectives of VIRGO, those of special interest for our work are: study the influence of solar active regions and other large-scale structures on total and spectral irradiance, study the solar energy budget, and provide accurate total and spectral irradiance data for input in terrestrial climate modelling.

VIRGO has three different types of sensors:

- two types of absolute radiometers (one DIARAD and two PMO6-V) for the measurement of total irradiance and its variations with high accuracy and precision,
- two 3-channel sunphotometers (SPM): the continuously exposed SPM is for the measurement of solar oscillations with high precision, the backup SPM for the measurement of the spectral irradiance with high accuracy and for corrections to the degradation of the continuously exposed instrument,
- one luminosity oscillation imager (LOI) for the measurement of the radiance in 12 pixels over the solar disk and the determination of the solar diameter.

Absolute radiometers are based on the measurement of a heat flux by using an electrically calibrated heat flux transducer. The radiation is absorbed in a cavity which ensures a high absorptivity over the spectral range of interest for solar radiometry. An electronic circuit maintains the heat flux constant by accordingly

controlling the power fed to the cavity heater. Both radiometers, DIARAD and PMO6-V, are based on the same principle but differ in the arrangements of the compensating cavities and the forms and coatings of those cavities. It is known from previous experiments that radiometers continuously exposed to the Sun degrade relatively to sensors that are exposed only occasionally. As a consequence at least one spare sensor is needed for each radiometer; DIARAD is using the compensating cavity and for PMO6-V a second instrument is included, increasing the redundancy.

The radiometers used in VIRGO are fully characterized and their measurements are individual realizations of the SI unit Wm^{-2}. Their absolute accuracy is $\pm 0.15\%$ for DIARAD (Crommelynck 1988) and $\pm 0.17\%$ for the PMO6-V (Brusa & Fröhlich 1986). The noises of PMO6-V and DIARAD have similar characteristics; for a single measurement, they are of the order of 30 ppm (parts per million).

The SPM has three independent channels at 402, 500 and 862 nm, with 5 nm bandwidth filters centered at the these wavelengths. The three detectors are mounted in a common body which is heated with constant power. This reduces degradation of the optical elements due to condensation of gaseous contaminants. One SPM is operated almost continuously, the dark current being checked only from time to time by shading the instrument with its cover. The other SPM is provided as a backup in case of failure of the first. Normally the second SPM is used to check for the possible degradation of the continuously exposed SPM. In the 5-minute range the noise power of SPM is about $10^{-6}\,\mathrm{ppm}^2\mu\mathrm{Hz}^{-1}$.

The LOI instrument is a solar photometer with very high stability that resolves the solar disk into 12 spatial elements. It consists of a 50 mm diameter, 1300 mm focal length Ritchey-Chrétien telescope, which provides a 12.5 mm diameter image. The solar image is projected on a Si photodiode array detector. The spectral bandpass is defined by a 5 nm bandwidth interference filter centered at 500 nm, which is placed in front of the detector. The Si detector (figure 2.3) has 12 scientific pixels and 4 guiding pixels. The precision for each pixel is about 1 ppm for an integration time of 10 s.

The 12 scientific elements are shaped specifically to allow detection of radiance variations and low-degree modes, while the other 4 elements constitute a guiding outer circular boundary of the detector. These guiding pixels are 4 quadrants of an annulus with an equivalent inner and outer radius of 0.95 and 1.05 $R_\odot$, respectively.

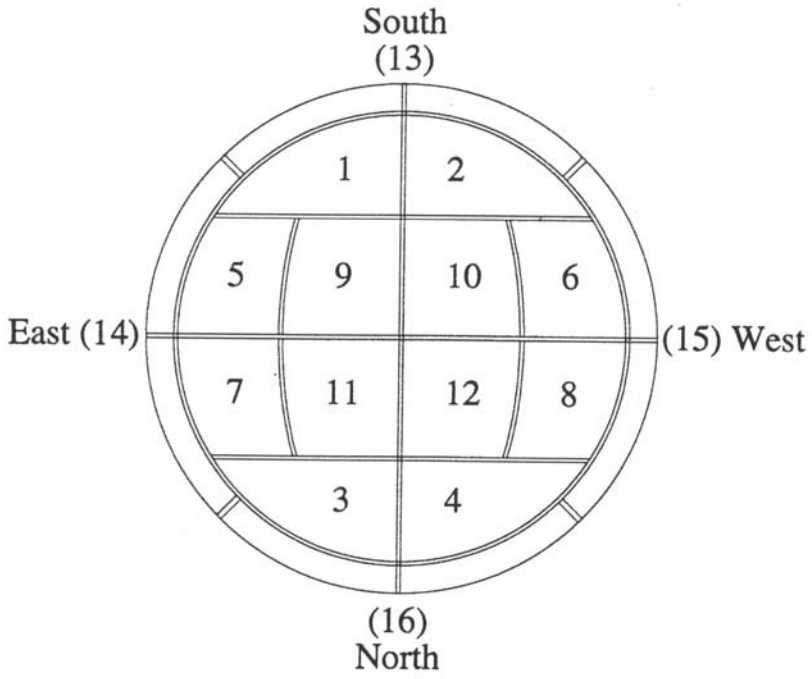

Figure 2.3: Configuration of the in-flight detector of the LOI with the correct orientation

The outputs of these four elements are amplified and, whenever the solar image exceeds the limits of the detector, error signals are generated to drive piezoelectric stacks, allowing the solar image to be stabilized within the limits of the detector. The signals of these four elements are also used to monitor the solar equatorial and polar diameters to better than $0.1''$.

2.1.2 The SOI/MDI experiment

The Solar Oscillations Investigation (SOI) uses the Michelson Doppler Imager (MDI) instrument to probe the interior of the Sun by measuring the photospheric manifestations of solar oscillations. The primary scientific objective of SOI is to measure the internal stratification and dynamics of the Sun using the techniques of helioseismology. Other scientific objectives include: study of the convection zone dynamics, internal rotation, study of the solar core, convection and large-scale flows, magnetic field measurements and study of the radiative flux budget. Of interest for our work are the radiative flux budget study and the magnetic field measurements. A very detailed description of the SOI/MDI instrument is given by Scherrer et al. (1995).

Table 2.3: MDI Observables and noise levels for a 1-minute measurement

Observable	Noise (1 σ)	Full Disk	High Resolution
Doppler Velocity	20 m/s	Yes	Yes
Continuum Intensity	0.3%	Yes	Yes
Line Depth	0.7%	Yes	Yes
Longitudinal Magnetogram	20 Gauss	Yes	Yes
Horizontal Velocity	30 m/s (8 hours)	No	Yes
Limb Position	0.02″ (5 minutes)	Yes	No

The Michelson Doppler Imager uses a refracting telescope to image sunlight through a cascade of increasingly narrow spectral filters onto a CCD camera. Two tunable Michelson interferometers define a 94 mÅ bandpass that can be tuned across the Ni I 6768 Å solar absorption line, and thus, obtain narrow-band filtergrams at five tuning positions 75 mÅ apart, spanning a tuning range of 377 mÅ. MDI records filtergrams, which are images of the solar photosphere in selectable, well-defined wavelength bands and polarization states. The filtergrams are used to derive the six key observables listed in table 2.3; estimates of the single measurement noise level are also given. These standard observables are computed from sets of five filtergrams, which are labeled F_0 through F_4. F_0 falls in nearly continuum, F_1 and F_4 are centered on the wings, while F_2 and F_3 are centered about the core of the Ni line. Among the six observables provided by MDI we are interested in both the photospheric continuum images and the magnetic field measurements. Longitudinal magnetograms are constructed by measuring the Doppler shift separately in right and left circularly polarized light. The difference between these two values is a measure of the Zeeman splitting, and it is roughly proportional to the magnetic flux density: the line-of-sight component of the magnetic field averaged over the resolution element.

MDI can observe in either of two spatial resolutions. The full disk (FD) mode has a field of view of $34 \times 34'$ with $4''$ resolution and pixel size of $2 \times 2''$. The high-resolution (HR) mode is magnified by a factor of 3.2 to provide $1.25''$ resolution ($0.625''$ pixel size) over an $11 \times 11'$ field of view. The detector system employs a 1024×1024 CCD that is read out at 500 000 pixels per second.

2.2 Data sets

VIRGO and MDI classify their data products as level 0, level 1 or level 2 data. Level 1 data are those that have been converted from raw counts (level 0 data) to physical units; they include calibrations and contain all the corrections known a priori for instrument-related effects, such as the influence of temperature variations. VIRGO signals are converted to flux measured at 1 AU, using the SOHO-Sun distance derived from the orbital data. In LOI, the correction takes into account the real shape of the 16 pixels, the limb darkening at 500 nm, and the in-flight size of the solar image at 1 AU. The pixels are also converted to zero radial velocity using the orbital data. Level 2 data are level 1 data corrected for degradation of the filters. For the total solar irradiance an average of the measurements with the two operational and the two backup radiometers is given.

MDI level 0 data have been calibrated into physical units; these calibration procedures constitute the Level 1 processing. The resulting Level 1 data products are typically the most basic scientifically useful data, and many scientific investigations can be conducted directly with level 1 images. The MDI data sets we are going to use belong to this level of processing. Others require level 2 processing, which need the observables to be decomposed into spherical harmonic modes.

In this thesis (Chapter 3) we have used those VIRGO data sets described in table 2.4. The data level is indicated in parenthesis. In some cases the SOHO-Sun distance was needed; this is given by the satellite telemetry at a cadence of 1 minute. Most of the work presented in Chapter 3 was carried out with LOI 0.7c data. These data are still level 0 data but some corrections have already been made (they have been converted to physical units, to flux measured at 1 AU and to zero radial velocity). In the next section we will describe the reduction method to convert LOI 0.7c data into level 2 data.

Chapters 4 and 5 are based on MDI data. All data sets belong to the level 1 data and are listed in table 2.5. In Section 2.4 the analysis procedures applied to MDI data will be described. All procedures to reduce and analyze VIRGO and MDI data, as well as all codes to derive the results presented, have been programmed using IDL language in conjunction with standard routines from the IDL SolarSoft package (Freeland & Bentley 1998; Freeland & Handy 1998).

Table 2.4: VIRGO data sets

Data set (level)	Resolution	Cadence	Time period
LOI (0.7c)	16 pixels	1 minute	April 1996 - April 1997
LOI (1.0)	16 pixels	1 minute	April 1996 - June 1998
SPM (1.0)	1 pixel, 3 wavelengths	1 minute	January 1996 - April 1997
Total Solar Irradiance	1 pixel	2 minutes	January 1996 - June 1998

Table 2.5: MDI data sets

Data set	Resolution	Cadence	Time period
fd_M_01h	Full Disk	1 minute	January 1999 - December 1999
fd_Ic_01h	Full Disk	1 minute	January 1999 - December 1999
fd_M_96m	Full Disk	96 minutes	May 1996 - November 2001
fd_Ic_01h	Full Disk	1 minute	May 1996 - November 2001

Data provided by the SOHO spacecraft have several advantages relative to those provided by ground-based observatories: they are not affected by seeing effects due to the Earth's atmosphere; they form an unprecedentedly large, continuous and homogeneous data set; the characteristics of the data sets are well known and stable; magnetograms and intensity images are obtained regularly by the same instrument with exactly the same spatial resolution. However, the full disk mode of MDI has a relatively low spatial resolution, and its measurements are available at only a single wavelength.

2.3 VIRGO data reduction

VIRGO raw data, i.e., level 0 data, cannot be analyzed straightforwardly, as solar irradiance or radiance variations become hidden by instrumental effects that must be corrected beforehand. How these corrections are performed is the subject of this Section.

LOI and SPM data were averaged every 96 minutes to simulate the cadence of MDI magnetograms. Total solar irradiance is given in 60 minute averages, and is already corrected from all distorting effects; therefore, it does not need any further reduction procedure. In this section we present the reduction method to convert

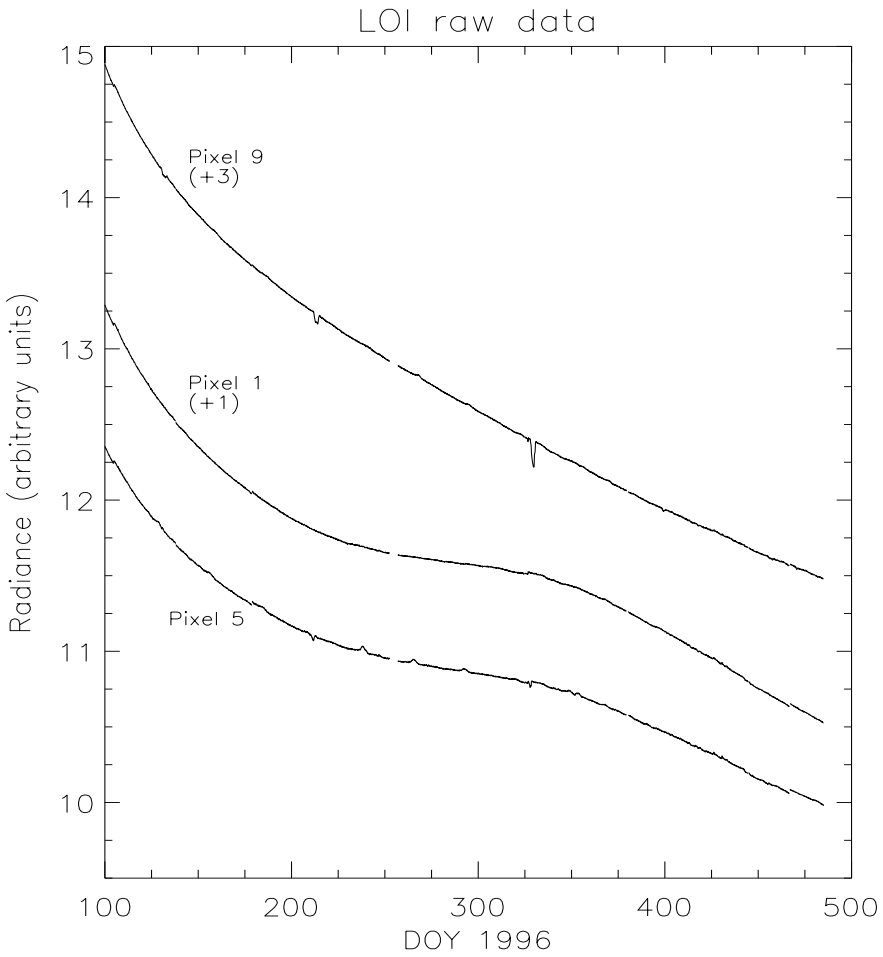

Figure 2.4: Level 0 (raw) LOI radiances from pixels 1, 5 and 9. Pixels 1 and 9 are to be added the value indicated in parenthesis. Solar radiance fluctuations are superposed to instrumental effects.

level 0 data from the VIRGO experiment into level 2 data. Figure 2.4 shows an example of LOI level 0 data. Small fluctuations due to the presence of active regions over the solar disk are superposed to the instrumental effects. Note that the variations due to solar activity are much smaller than the downward trend caused by instrument-related effects, therefore any physical interpretation from these data requires previous reduction and correction of the distorting effects.

2.3.1 Variation of the limb darkening with distance

Observations resolving the solar disk are affected by the limb darkening effect. This effect is wavelength dependent, and it is due to radiation coming from different

heights of the solar atmosphere. For a detailed explanation see Mihalas (1970).

The distance between the SOHO spacecraft and the Sun varies throughout the year due to its orbit around the Sun and to its halo orbit around L1. The variation in distance ranges between 0.973 and 1.007 AU. Because of this annual variation, the portion of solar disk observed by each LOI scientific pixel changes with time. If, for example, the SOHO-Sun distance increases, then the area of solar disk observed by a given pixel also increases; this implies increasing the amount of limb darkening affecting that pixel and, as a consequence, the intensity gradient between the two limits of the pixel increases. Central pixels, (i.e. pixels 9, 10, 11 and 12 in figure 2.3), measure a lower intensity gradient as their observed portion of disk increases. Side pixels (i.e. pixels 5, 6, 7 and 8), which observe closer to the limbs, are affected by a higher intensity gradient. The reason for this response is the non-linearity of the limb darkening effect. In the next paragraphs we describe the method used to correct for the limb darkening variation with distance.

Appourchaux & Telljohann (1996) proposed a correction for the limb darkening variation with distance, following the limb darkening function given by Neckel & Labs (1994). They used this function to derive the limb darkening affecting the surface of each pixel, by integrating over the exact shape and position of the given pixel on the Si array, for different distances. The final output is a fitted correction function, C(d), of the form:

$$C(d) = 1.0 + a\Delta\mathrm{d} + b\Delta\mathrm{d}^2 \tag{2.1}$$

where Δd means the distance (in AU) to the mean Sun-Earth orbit, counted positively away from the Sun (Δd=d-1). The coefficients a and b, given in table 2.6, include the intrinsic characteristics of each pixel.

We tried other methods to correct for the limb darkening variation with distance. Even when they were simpler than that proposed by Appourchaux & Telljohann (1996), the results proved to be very similar. See Ortiz (1999) for details about these methods.

The limb darkening-distance correction is only to be applied to LOI data because LOI is the only VIRGO detector producing an image of the Sun. The SPM instrument and the absolute radiometers do not resolve the solar disk and therefore

Table 2.6: Coefficients for the limb darkening-distance correction

Pixels	a	b
1 to 4	-1.0805	-2.8714
5 to 8	-0.8990	-2.1797
9 to 12	-0.1091	-0.0786
13 to 16	-24.6500	100.3311

this correction is not applicable. For a more detailed approach see Ortiz (1999).

All irradiance and radiance measurements are normalized to 1 AU. Other instrumental distortions (Appourchaux et al. 1995) already corrected are the Doppler effect due to the line-of-sight velocity and, in LOI, the temperature effect on the detector, due to the temperature sensitivity of the quantum efficiency of the silicon detector.

2.3.2 Instrumental degradation

2.3.2.1 LOI

Instrumental sensitivity decays with time because UV radiation and energetic particle fluxes degrade the entrance windows and filters of the detectors. The window or filter opacity can increase as a result of contaminant accumulation and plastic decomposition. An example of such degradation was the SOVA2 experiment during the EURECA mission (Wehrli et al. 1995). Because EURECA was retrieved, the SOVA2 sunphotometers could be analyzed after the flight. A significant amount of degradation was attributed to a brownish stain deposited on the entrance window, most probably due to molecular contamination photopolymerized by the strong UV radiation.

After removal of the effects described in previous sections, LOI and SPM data are still affected by a downward trend produced by filter degradation. Figure 2.5 presents an example of data for pixels 5 and 9, still not corrected for instrumental degradation. As can be seen, the annual fluctuation in the original data produced by the limb darkening variation with distance (specially in pixel 5) has disappeared.

Assuming that all downward trend is due to filter degradation, detrended data should eventually be free from instrumental distortions, and therefore can be considered as level 2 data. Resulting data sets are expected to be a measure of the quiet Sun background distorted by fluctuations caused by the passage of active regions.

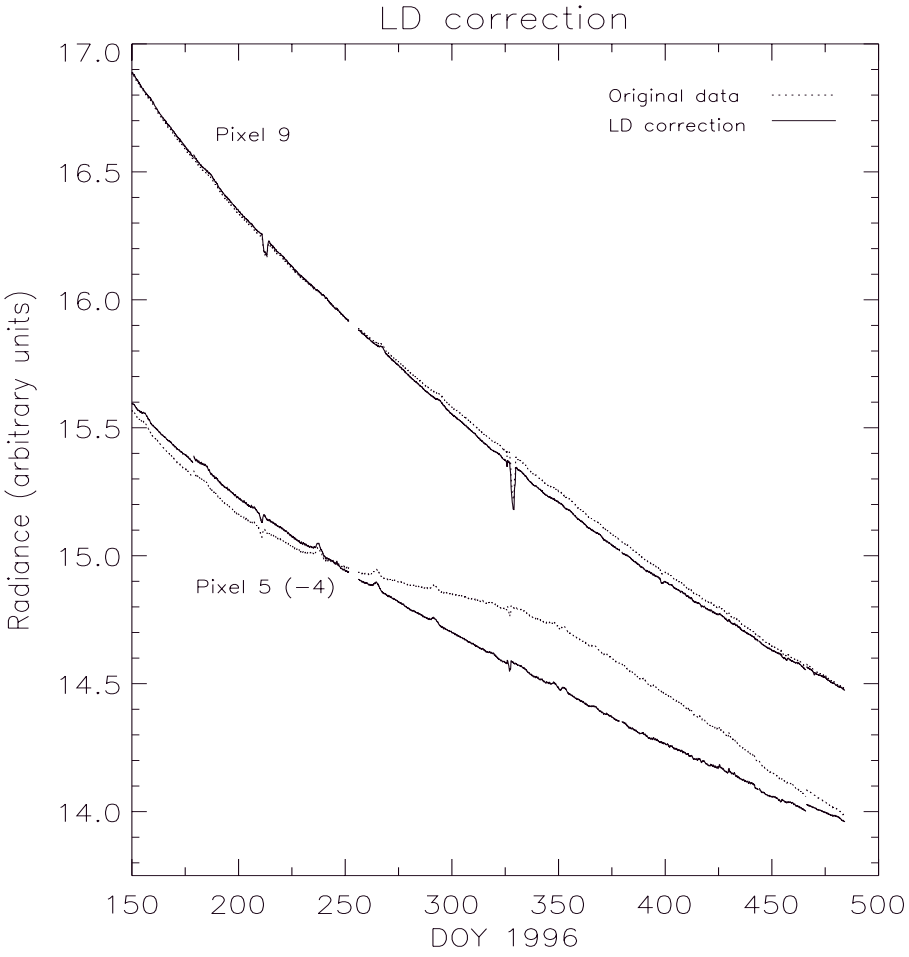

Figure 2.5: Correction for the limb darkening variation with distance in two of the LOI pixels. Pixel 5 is to be added the value in parenthesis. Dots represent original data (level 0) and the solid curve represents data corrected for limb darkening (level 1) according to Appourchaux & Telljohann (1996).

The data were detrended by means of least-squares fits to irradiance measurements. The time period studied extends from April 1996 to April 1997 for LOI 0.7c, and from January 1996 to April 1997 for SPM 1.0. We have fitted exponential functions as well as polynomials whose degree ranged from 1 to 9. Fifth degree polynomials gave the best results for LOI data, as they minimized the differences

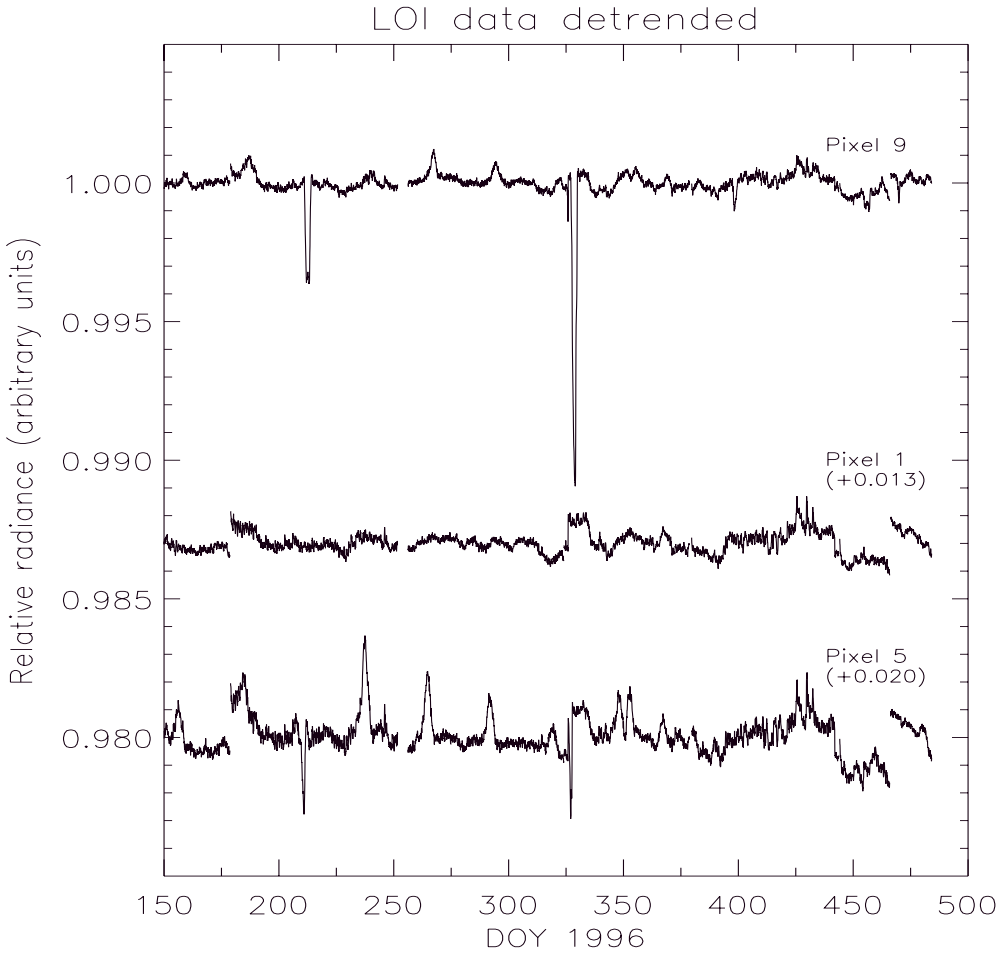

Figure 2.6: LOI pixels 1, 5 and 9 relative radiances corrected from instrument-related effects. Pixels 1 and 5 are to be added the values in parenthesis. Fluctuations due to the presence of active regions can now be easily observed relative to a quiet Sun background.

with the observations. Our results are in accordance with the conclusions reached by Wehrli et al. (1998).

These fits are only intended to reproduce the instrumental degradation, therefore once the best fit for each pixel has been determined, we remove intervals lacking data, or intervals presenting radiance fluctuations due to the presence of active regions. The process is repeated for each LOI pixel to model its specific degradation. Table 2.7 presents the coefficients of the best quintic fit to each pixel, a_i (where i runs from 0 to 5), together with their uncertainties σ_{a_i} and the standard deviation between data and model.

Table 2.7: Quintic polynomial fitting to LOI pixel degradation.

	$a_0 \pm \sigma_{a_0}$	$(a_1 \pm \sigma_{a_1}) \cdot 10^{-2}$	$(a_2 \pm \sigma_{a_2}) \cdot 10^{-4}$	$(a_3 \pm \sigma_{a_3}) \cdot 10^{-6}$	$(a_4 \pm \sigma_{a_4}) \cdot 10^{-9}$	$(a_5 \pm \sigma_{a_5}) \cdot 10^{-12}$	σ_{fit}
Pixel 1	16.40 ± 0.03	-3.53 ± 0.05	1.44 ± 0.03	-0.34 ± 0.01	0.39 ± 0.02	-0.15 ± 0.01	0.004
Pixel 2	16.67 ± 0.03	-4.03 ± 0.04	1.81 ± 0.03	-0.47 ± 0.01	0.60 ± 0.01	-0.31 ± 0.01	0.004
Pixel 3	16.55 ± 0.02	-3.81 ± 0.04	1.65 ± 0.03	-0.41 ± 0.01	0.50 ± 0.01	-0.24 ± 0.01	0.004
Pixel 4	16.51 ± 0.02	-3.72 ± 0.04	1.57 ± 0.03	-0.38 ± 0.01	0.45 ± 0.02	-0.23 ± 0.01	0.004
Pixel 5	13.90 ± 0.03	-2.46 ± 0.05	0.83 ± 0.04	-0.15 ± 0.01	0.10 ± 0.02	0.02 ± 0.01	0.005
Pixel 6	14.19 ± 0.02	-3.07 ± 0.05	1.28 ± 0.03	-0.31 ± 0.01	0.37 ± 0.02	-0.17 ± 0.01	0.005
Pixel 7	13.83 ± 0.03	-2.39 ± 0.05	0.80 ± 0.03	-0.15 ± 0.01	0.10 ± 0.02	0.02 ± 0.01	0.005
Pixel 8	14.11 ± 0.03	-2.95 ± 0.04	1.22 ± 0.03	-0.30 ± 0.01	0.36 ± 0.02	-0.16 ± 0.01	0.004
Pixel 9	21.82 ± 0.02	-6.80 ± 0.04	3.68 ± 0.03	-1.10 ± 0.01	1.70 ± 0.01	-1.10 ± 0.01	0.004
Pixel 10	22.05 ± 0.02	-7.23 ± 0.04	4.00 ± 0.03	-1.20 ± 0.01	2.00 ± 0.01	-1.13 ± 0.01	0.003
Pixel 11	21.85 ± 0.02	-6.91 ± 0.04	3.77 ± 0.03	-1.10 ± 0.01	1.70 ± 0.01	-1.12 ± 0.01	0.004
Pixel 12	21.91 ± 0.02	-6.97 ± 0.04	3.82 ± 0.03	-1.10 ± 0.01	1.80 ± 0.01	-1.10 ± 0.01	0.004

The final step is to normalize each pixel radiance by its degradation function. These detrended relative radiances are corrected from all known instrumental effects, becoming level 2 data. Figure 2.6 shows the temporal evolution of the radiance for pixels 1, 5 and 9, converted to level 2 data. Now the variations induced by the passage of sunspots and faculae over the solar disk can be easily seen superposed to a relative quiet Sun background. This temporal evolution can be compared with that of figure 2.4.

2.3.2.2 The polynomial fitting, FFT and PPN algorithms

The fact that degradation of the detectors follows a polynomial law does not have a clear physical meaning, and that makes us feel uncomfortable. Therefore, we attempted to detrend data using other algorithms. First we used FFT (Fast Fourier Transform) algorithms to create a high pass filter with a cutoff frequency of 27 days^{-1} and applied a Parzen (triangular) window (T. Appourchaux, private communication). This filter passes high frequencies (> 27 days^{-1}) and therefore short period oscillations due to solar activity, and filters out long term oscillations (low frequencies), such as downward trends in the data due to the aging of the detectors.

This procedure has the advantage that no assumption is made about the degrading behaviour of the filters, as with the least-squares fit. The main disadvantage is that FFT algorithms do not work whenever the input time series includes discontinuities (i.e., lack of data). Even replacing the gaps by interpolation of neighbouring data results in edge effects around the discontinuity. The algorithm also produces distortions when original data present abrupt variations, due for example to the passage of a huge sunspot; in figure 2.7 we plot LOI data as a function of time detrended by the FFT algorithm. Note the behaviour of the algorithm in the focused areas. Left panels show the original time series where some data are lacking. The FFT algorithm presents edge effects in the limits of the gap. Right panels show the passage of a sunspot that produces a deep dip in intensity. The FFT responds with abnormal fluctuations and a false increase in the intensity (a *false* facula).

Another hand-made algorithm to detrend LOI data is based in the hypothesis that polar pixels (1, 2, 3 and 4 in figure 2.3) hardly detect any solar activity because they point to the polar regions of the Sun, far away from the activity belt. This assumption is valid, at least during the period analyzed. The signal detected by

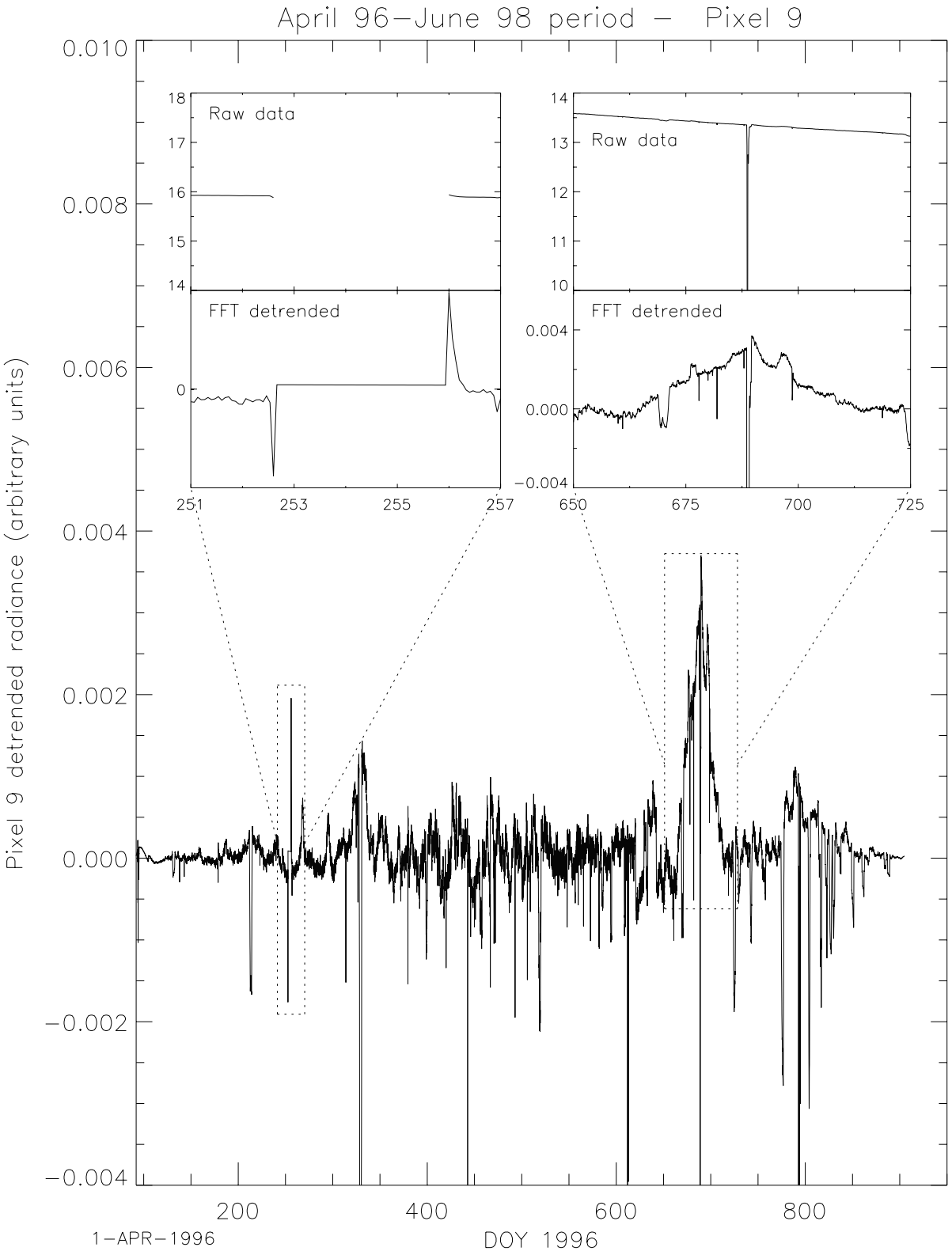

Figure 2.7: Detrending of LOI pixel 9 radiance using the FFT algorithm. Note the abrupt behaviour yielded by this method whenever raw data present any kind of discontinuity (see focused areas).

the polar pixels is then almost free from variations induced by activity and only reproduces the degradation. If we assume that all pixels degrade in the same manner, dividing one pixel signal by the sum of the polar pixels results in a detrended radiance. Therefore, this algorithm considers the radiance of a given pixel divided by the sum of the radiances of the four polar pixels. We will call this method the polar pixel normalization, or PPN.

We now compare the three methods (fifth degree polynomial fit, FFT and PPN algorithms) and illustrate them with an example. As mentioned in table 2.4, our LOI 1.0 data sets extend from April 1996 to June 1998. Since they are level 1 data, only degradation of the filters has to be removed. Applying those procedures to this 27-months period we obtain the following:

- **Polynomial fitting.** The results are worse than when applied to a shorter period of time (LOI 0.7c data set). Two time intervals can be identified according to their different degradation rates, from April to June 1996, and from June 1996 to June 1998. The first part presents a much steeper degradation, while the second part is considerably flatter. This makes it difficult to derive a single function that fits both intervals reasonably well. In short, the quintic least-squares fit yields good results when applied to a short time interval, i.e., one year or less. The period in which we are interested in Chapter 3, July 1996 to November 1996, falls within the range of LOI 0.7c data, being adequately detrended by this method.

- **FFT algorithm.** When applied to LOI 1.0, FFT yields abnormal fluctuations, because the data set contains discontinuities that cannot be removed by this method.

- **PPN algorithm.** This method produces the best results for longer periods. However, we must be very careful when choosing the time interval, because solar activity increases considerably at the end of 1997, when even pixels 1, 2, 3 and 4 detect the passage of active regions. This activity would then jeopardize the result of the normalization. In the period covered by LOI 1.0 data, this effect is evident, for example, in Carrington rotation 1926 (see Appendix B).

Figure 2.8 illustrates how the polynomial fit and the polar pixel normalization remove degradation from LOI data. The plot shows Carrington rotation 1912 (from

25 July 1996 to 22 August 1996), one of the solar rotations of interest for the study carried out in Chapter 3. The correction yielded by the polar pixel normalization is better than the polynomial fitting as it provides flatter backgrounds.

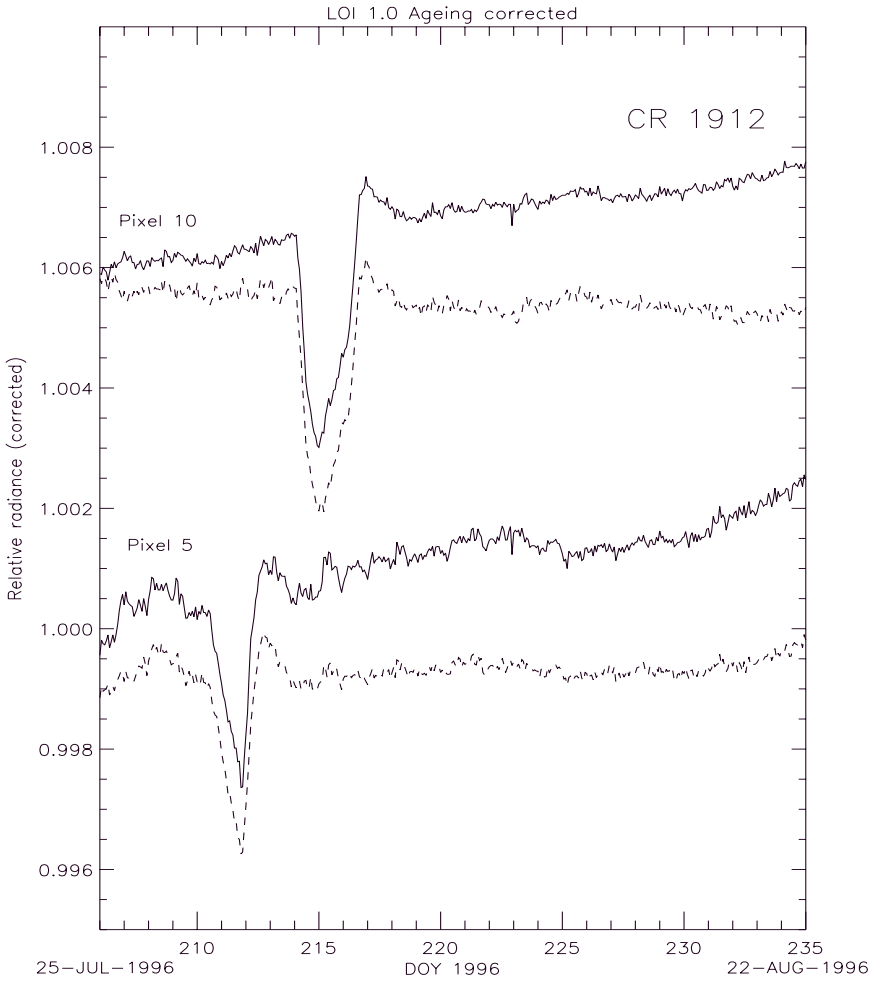

Figure 2.8: LOI 1.0 data (pixels 5 and 10) detrended by means of two methods: fifth degree polynomial fitting (solid line) and polar pixel normalization (dashed line), for Carrington rotation 1912. For clarity, radiances have been separated by 0.005 arbitrary units. Polar pixel normalization detrends better the data.

From this analysis, we conclude that it is necessary to refine the procedures to correct data from aging of the filters and entrance windows. But the fact that we have no previous knowledge of the aging behaviour of the detectors, and that we cannot have access to them, makes this task very complicated.

2.3.2.3 SPM sunphotometers

The procedure followed for the three spectral channels of the SPM sunphotometers is similar to that used for LOI. SPM data sets are level 1 data, in which the only procedure to be applied is the degradation correction. Figure 2.9 presents the downward trend showed by each spectral irradiance as a function of time. Note that the degradation rate is not the same for the three spectral channels, because different filters are used in each channel. The filter that shows most degradation is the blue (402 nm) while the least affected is the red channel (862 nm).

We have also tried several functions to fit the decrease in the irradiance. The best fitting functions turned out to be third degree polynomials for the 862 nm channel, and fourth degree polynomials for the 500 and 402 nm channels. Again, we have excluded intervals with no data or containing solar activity. Figure 2.10 presents the temporal evolution of the resulting SPM level 2 data; the relative detrended irradiances now show the signature of solar activity very clearly, superposed to a flat quiet Sun background.

2.3.3 Calibration

Table 2.8: Reference solar spectrum

	402 nm	500 nm	862 nm
Spectral irradiance ($\mathrm{mW\,m^{-2}nm^{-1}}$)	1794	1935	1046

Spectral irradiances are not directly comparable, as the Sun does not radiate the same energy flux in every wavelength. It is necessary to calibrate spectral irradiances with the reference solar spectrum to compare measurements, which allows conversion of the measurements into SI realizations, $\mathrm{mW\,m^{-2}nm^{-1}}$. This calibration was lost in the data conversion to level 2. Table 2.8 gives the values of the reference spectrum at the wavelengths studied (taken from Thuillier et al. 1998). Total solar irradiances are absolute and bolometric measurements, and do not require any further calibration. SPM and LOI data are now measurements relative to the quiet Sun background.

There is still another calibration for LOI pixels. Pixels measure different signals, depending on their size and position over the Si array. Specifically, pixels pointing

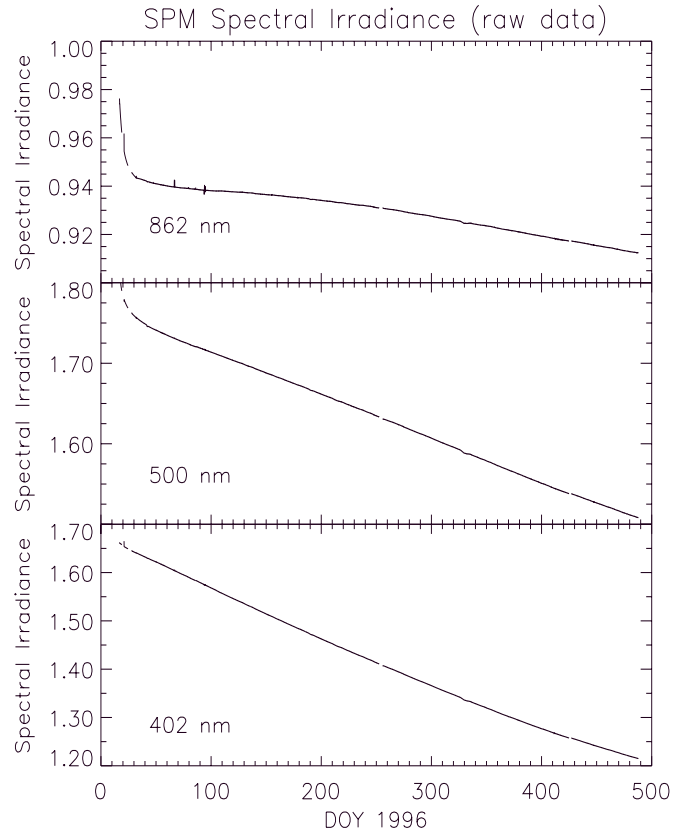

Figure 2.9: SPM raw data as a function of time. Note the different degradation rate for each filter.

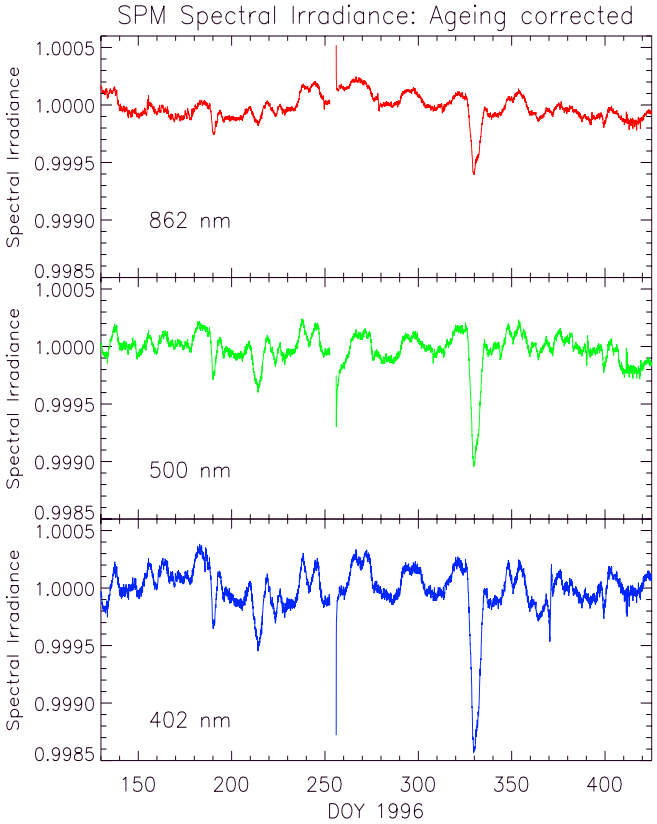

Figure 2.10: Relative SPM spectral irradiances corrected from filter degradation. Degradation of the red channel has been fitted by a third degree polynomial; green and blue channels have been fitted by fourth degree polynomials. The spectral channels detect the passage of active regions.

to the center of the disk (pixels 9, 10, 11 and 12 in figure 2.3) receive more radiance, while those at the sides (5, 6, 7 and 8) receive less signal. These differences can be seen in figure 2.4, which shows the diversity of signals depending on the pixel. After correction of the limb darkening variation with distance and of the degradation of the filters, all pixels have been normalized to the quiet Sun background, hiding the original relations between pixels. Each pixel can be recalibrated in order to recover its original weight within the photodiode array; this is done considering the original relations between pixels.

The reduction process of the VIRGO data sets ends with these calibrations. Figure 2.11 is an example of LOI level 2 data for three Carrington rotations. At this stage, data can be analyzed and physically interpreted; we do this in Chapter 3.

2.4 MDI data analysis

The analysis of MDI data is different from that carried out for VIRGO data. Our MDI data sets belong to level 1, and therefore do not need to be corrected for instrument-related effects. Nevertheless, the determination of the contrast of small magnetic elements requires analytical procedures in order to identify the surface distribution of solar magnetic features that produce a bright contribution to irradiance variations. Among the observables provided by MDI, we are interested in both continuum images and magnetic field measurements. Figure 2.12 shows a simple MDI data analysis flow chart illustrating the interactions between the different IDL routines created to analyze MDI data sets, as well as the sequence followed in their usage. Each routine indicates its utility, the necessary inputs and the outputs provided.

First, we calculate the position of each pixel over the solar disk, $\mu(x, y)$, (program MU.PRO), which is characterized by μ ($\mu = \cos\theta$, where θ is the heliocentric angle). The 1-σ noise level of the MDI magnetograms is computed using the program NOISE_MAG.PRO. This is a key step, as the selection of disk features depends entirely on these noise levels. The MDI data sets used in Chapters 4 and 5 have their own peculiarities, and so we will report the noise levels specifically determined for each case in those chapters. Here we will describe the general guidelines followed.

The noise level of the magnetograms, $\sigma_{\rm mag}$, is calculated for all CCD pixels, thus

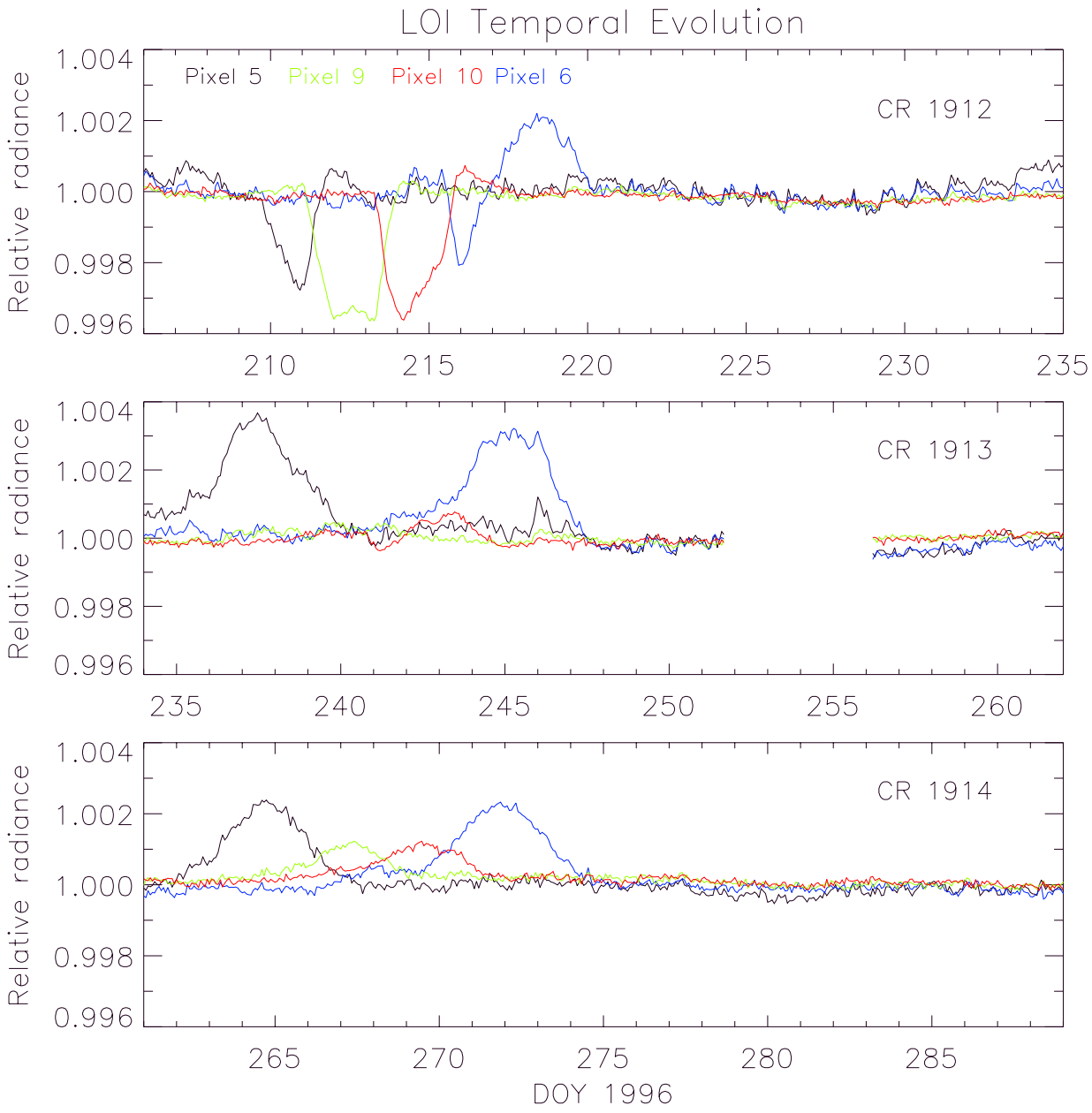

Figure 2.11: Relative radiance temporal evolution measured by LOI for Carrington rotations 1912, 1913 and 1914. Pixels 5, 9, 10 and 6, now free from instrument-related effects, detect succesively the passage of an isolated active region.

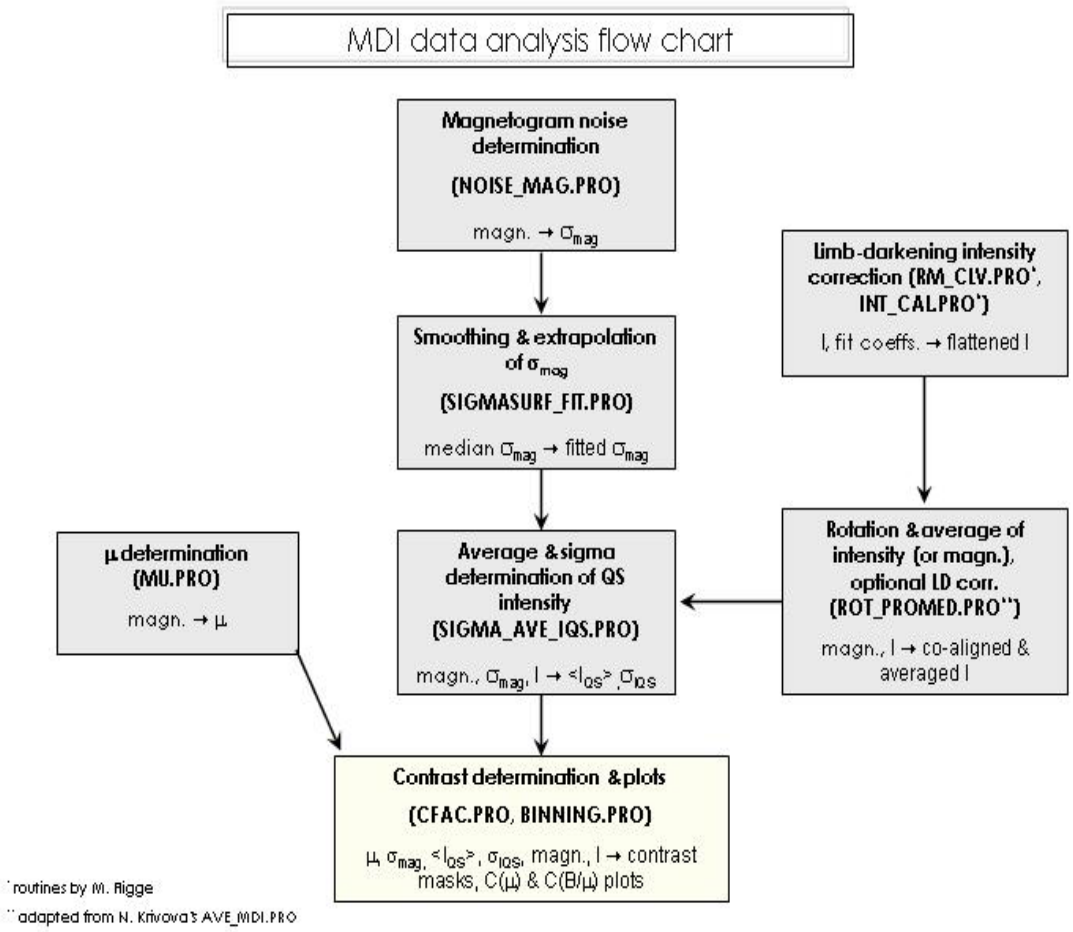

Figure 2.12: MDI data analysis flow chart illustrating the interactions between routines and the sequence of their usage. In each routine we indicate the inputs (I) and outputs (O) of the procedure in the form: I $\rightarrow$ O.

Table 2.9: Selected days and times (hours/min/sec) during 1996 at which quiet Sun magnetograms were recorded.

1996 observation dates	Time (UT)
July 18	01:40:05
September 10	16:03:04
September 11	16:03:04
October 6	03:15:04
October 8	14:27:04
October 10	11:15:04
October 12	16:03:04
October 15	19:15:04
October 16	19:15:04
October 31	00:03:04
November 1	16:03:04
November 5	12:51:04
November 6	16:03:05
December 4	16:03:05
December 6	09:39:05
December 30	09:39:05

giving a map of the standard deviation, $\sigma_{\rm mag}(x, y)$, where x and y are the coordinates of a given pixel. This determination needs to be performed using magnetograms with the least possible solar activity (or removing it), as our aim is to measure the noise produced by the instrument itself. As a consequence, we selected 16 quiet Sun magnetograms from 1996 (see table 2.9), almost free from solar activity.

The standard deviation of the magnetic signal as a function of position over the CCD array was calculated by means of a running 100×100 pixel box over the solar disk, with the exception of the limbs, which were avoided by masking out an outer ring of 75 pixels width. Several sizes were tried for this box, from 10×10 to 200×200 pixel size. Too small boxes yielded a high scattering map. On the other hand, too large boxes were really time consuming and could even mask the limb variation presented by the noise; we will return to this point later. We found that 100×100 pixel boxes is a fair compromise between calculation time and removing scattering without masking out intrinsic properties of $\sigma_{\rm mag}(x, y)$. Once $\sigma_{\rm mag}$ was calculated for the 16 magnetograms following this method, we calculated the median of all 16 standard deviation maps to avoid possible remaining daily fluctuations. Next, we fitted a smoothing second order surface to this map and extrapolated it to cover the

whole solar disk (program SIGMASURF_FIT.PRO; this script uses the SFIT IDL routine for surface fitting). The fitted surface is:

$$\sigma_{\rm mag}(x,y) = 9.19 + 2.40\,10^{-3}x - 7.42\,10^{-4}y + 3.11\,10^{-6}x^2 - 1.43\,10^{-6}y^2 \qquad (2.2)$$

This surface minimizes the differences with respect to the median. The resulting noise map, as shown in Chapter 4 (see figure 4.2), presents an increase towards the SW limb that probably includes some velocity signal leakage. Liu & Norton (2001) found a 9 G level for the 5 minute magnetograms, assuming that the low-level signal is purely noise.

According to Liu & Norton (2001) the noise in the magnetograms originates from two main components: photon shot noise and leakage from the Doppler signal. The shutter noise introduces a 0.5 G uncertainty. These authors analyzed MDI measurement errors and found that MDI underestimates velocity and magnetic field up to 5% and 15%, respectively. The level of underestimation depends on both the field strength and disk position, being the strong-field regions (> 2000 G) most affected. The investigations we carry out do not include such field strengths, as we have an upper limit of 600 G.

In Chapters 4 and 5 we examine simultaneous or near-simultaneous pairs of magnetograms and photospheric continuum intensity images. All intensity images have been corrected for limb-darkening effects using a fifth order polynomial in μ as suggested by Neckel & Labs (1994) (programs RM_CLV.PRO and INT_CAL.PRO; M. Fligge, private communication). Intensity images have also been rotated to co-align them at the same time as their corresponding magnetogram (program ROT_PROMED.PRO, adapted from N. Krivova's AVE_MDI.PRO, private communication). The importance of such rotation is illustrated in figure 2.13. Figure 2.13a shows an active region on a magnetogram taken on June 7, 1998 at 03:15:04 UT. Figure 2.13b shows its corresponding intensity image, taken 45 minutes earlier, at 02:30:34 UT. The green vertical line indicates the position of the minimum intensity produced by the sunspot. Figure 2.13c presents the same intensity frame rotated 45 minutes (3.5 pixels) to co-align it with the magnetogram. The red vertical line indicates where the dip in intensity lies after rotation. It fits with the center of the magnetic concentration associated with the sunspot. Now, active features overlap in both the magnetogram and intensity frames, and both types of images can be compared pixel by pixel. This procedure can be used (optionally) to create averages over several MDI magnetograms or intensity images, rotating the images first to

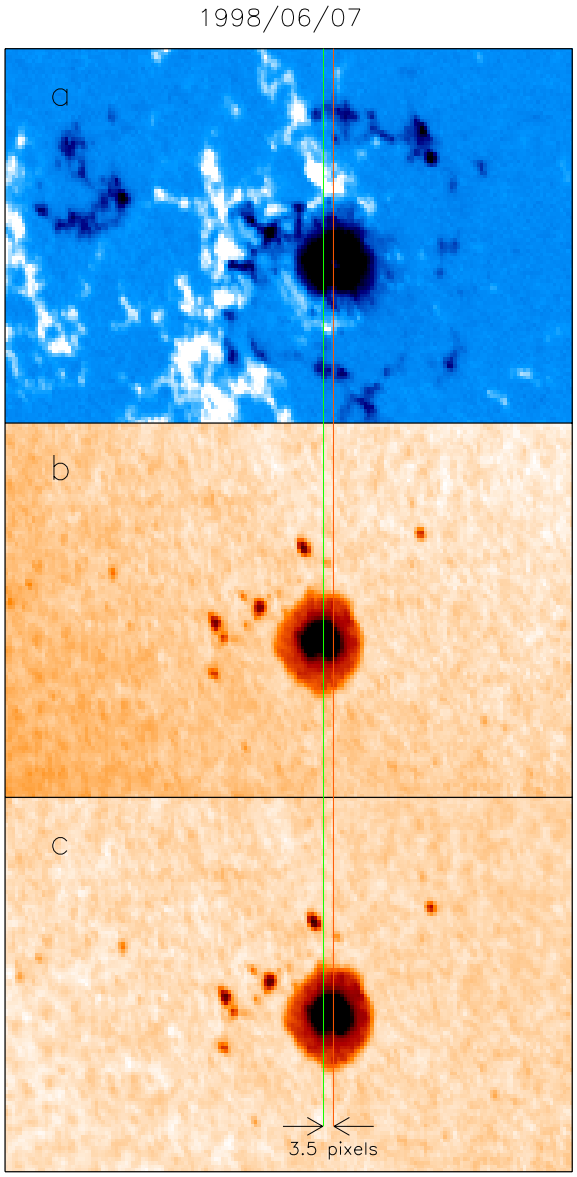

Figure 2.13: **a)** Magnetogram taken on June 7, 1998 at 03:15:04 UT; **b)** Intensity counterpart, taken 45 minutes apart, at 02:30:34 UT; **c)** Same intensity snapshot that has been rotated 45 minutes (3.5 pixels following the rotation of the Sun). The green line indicates the dip in intensity before rotation. The red line marks the dip in intensity after co-alignment. After rotation, features overlap in the magnetogram (a) and intensitigram (c), allowing detection of solar activity.

some reference image in order to correct for differential rotation. Averaging magnetograms is important in order to increase the signal-to-noise ratio, as more network features become visible when going to longer averages or, equivalently, longer integration times. Fligge et al. (2000a) show the effect of the averaging on the detection of the active network in figure 3 of their work; from this figure we can affirm that averaging series of 5 or 20 consecutive magnetograms enables a more reliable detection of network features.

We have also derived the mean and standard deviation of the quiet Sun continuum intensity for each image, $\langle I_{\rm qs}\rangle(x,y)$ and $\sigma_{\rm Iqs}(x,y)$ respectively; the subscript qs denotes "quiet Sun". The method is similar to the determination of $\sigma_{\rm mag}(x,y)$ (program SIGMA_AVE_IQS.PRO). We used running mean boxes with a size of 100×100 pixels, except close to the limits of the CCD array, where $2d\times2d$ boxes were used (being d the distance from a given central pixel to the limit of the array). Pixels in the running box with an absolute magnetic signal value below 0.5 times $\sigma_{\rm mag}$ have been considered as "quiet Sun" pixels. Those pixels are then identified in the intensity image, and their mean and standard deviation are derived according to the running box method (again, this is a time-consuming process). Maps of the mean quiet Sun intensity are intended as a background intensity when no activity is present over the solar disk. Figure 2.14 shows an example of such maps. Note that the background intensity is not flat, presenting variations of about 2%, probably due to the approximate correction of the limb-darkening effect.

The last step is to select pixels which present magnetic activity and are associated with bright contributions to irradiance variations; in this way we exclude sunspots and pores from our calculations. These points are identified by setting two thresholds to every pair of magnetogram and intensity image (program CFAC.PRO). The first threshold looks for magnetically active pixels; a pixel is considered magnetically active when its absolute magnetic signal value is above $3\sigma_{\rm mag}$. The value of this threshold depends on $\sigma_{\rm mag}$, which in time depends on the averaging of MDI magnetogram series. We have tested several thresholds, from $\sigma_{\rm mag}$ to $4\sigma_{\rm mag}$, concluding that the best identification results were achieved when taking the $3\sigma_{\rm mag}$ threshold. Lower thresholds selected magnetic activity together with many salt-and-pepper pixels, specially from the SW limb where the noise seems to be higher (see figure 4.2); the $4\sigma_{\rm mag}$ threshold missed some features that could not be identified as noise.

The second threshold masks out sunspots and pores by setting all pixels with a

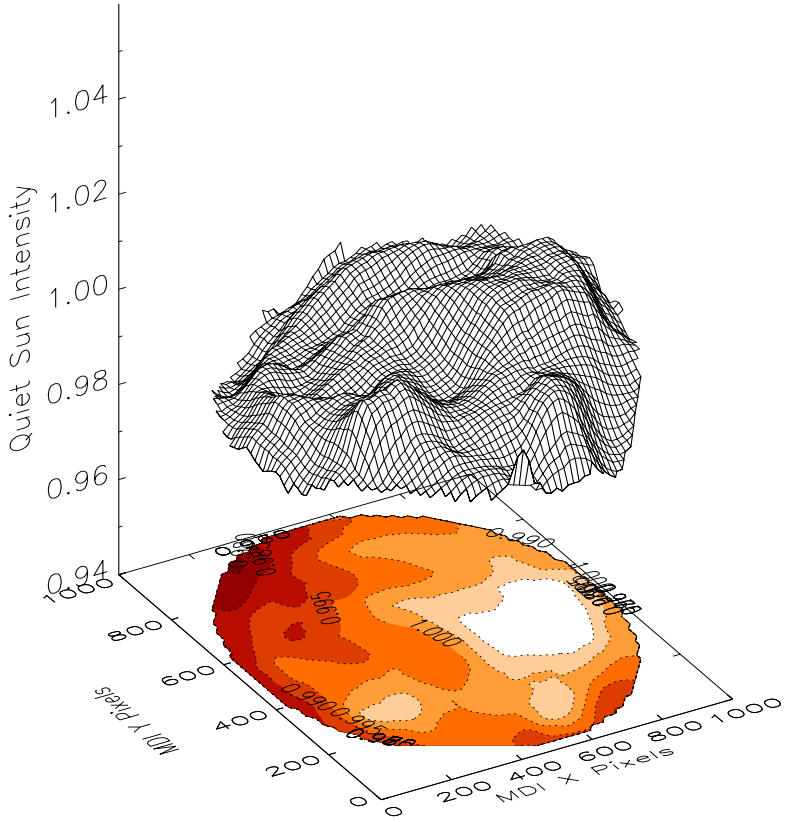

Figure 2.14: Mean quiet Sun intensity map (arbitrary units) for February 20, 1999. The shadowed contours indicate some of the values. Both the surface and the contours represent the mean intensity. Variations of around 2% are present in this background intensity.

continuum intensity $3\sigma_{\mathrm{Iqs}}$ below the average to a null value. We again tested several thresholds. In summary, our final selection includes points fulfilling the magnetically active condition, but not the sunspot condition.

In order to reduce false detections we set two additional filters to reject noise and extreme limb points. We rejected all isolated pixels above the given thresholds assuming that they were noise, even at the risk of missing pixels. In addition, points belonging to the extreme limbs ($\mu \leq 0.14$) were removed to avoid strange detections at the image limits. After applying these criteria, we found that about 6% of the pixels in each magnetogram-intensity pair satisfied them.

Once the surface distribution of solar magnetic features has been identified for each magnetogram-intensity pair, we determine their contrast (program CFAC.PRO). For a pixel with coordinates (x, y), the contrast $C_{\rm fac}$ is defined as:

$$C_{\rm fac}(x,y) = \frac{I(x,y) - \langle I_{\rm qs}\rangle(x,y)}{\langle I_{\rm qs}\rangle(x,y)} \tag{2.3}$$

At this point, we constructed a mask of the contrast of bright features. These masks indicate the surface distribution of magnetic activity present over the solar disk at a given moment and its associated contrast. In figure 2.15 we show sample magnetograms (top), photospheric continuum intensities (middle) and their derived contrast masks (bottom) for three days during the rising phase of solar cycle 23. Note that only features lying above the given thresholds are pinpointed as black pixels; sunspots, for example, do not appear in the masks, but their surrounding faculae are identified.

For each pair of MDI longitudinal magnetogram and photospheric intensity, pixels are selected according to the aforementioned conditions. Contrast, magnetic field and position, represented by the heliocentric angle $\mu = \cos\theta$, are calculated for each of those pixels. Selected pixels from different days are put together to build long temporal series, which provide adequate statistics for a detailed study of the facular and network contrast. Finally, the program CFAC.PRO can represent the contrast $C_{\rm fac}$ both as a function of position and as a function of magnetogram signal. This results will be presented and discussed in the next Chapters.

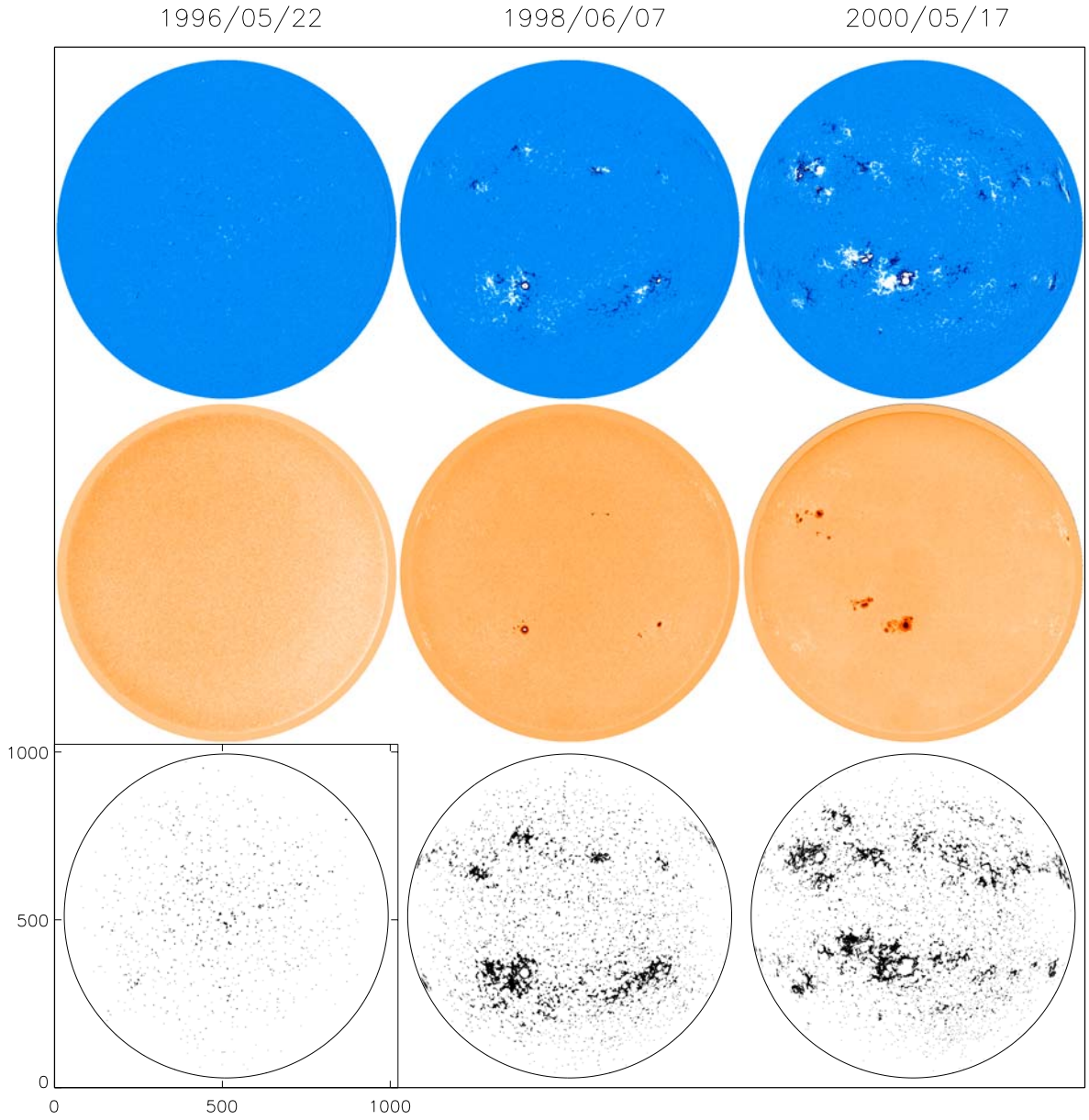

Figure 2.15: Three examples of MDI magnetograms (top panels), their corresponding intensity images after removal of limb-darkening (middle panels), and the resulting contrast masks (lower panels) for May 22, 1996 (left), June 7, 1998 (middle) and May 17, 2000 (right). One can see the increasing activity present over the solar disk as the maximum of solar cycle 23 is reached. A circle indicates the size of the Sun in each contrast mask.